Mechanism of titanium electrochemical oxidation *via* isotopic labeling, high resolution ion depth profiling, and impedance spectroscopy

M. Brocklebank [a], H. Feltham [b], J.J. Noël [b], L.V. Goncharova [a],*

[a] *Department of Physics and Astronomy, Western University, London, Ontario N6A 3K7 Canada*
[b] *Department of Chemistry, Western University, London, Ontario N6A 3K7 Canada*

ARTICLE INFO

ABSTRACT

The electrochemical oxidation mechanism of titanium between 0 and 10 V vs saturated calomel reference electrode (SCE) was examined for ultra-thin Ti films sputtered onto Si(001) substrates and exposed *in-situ* to $H_2^{18}O$, and then anodized in $D_2^{16}O$. The effects of this isotopic labeling procedure were studied using medium energy ion scattering (MEIS) and nuclear reaction profiling (NRP). Both MEIS and NRP results are consistent in showing that the titanium oxide layer is composed of two distinct regions, $Ti^{16}O_2/Ti^{18}O_2/Ti/Si(001)$ for the entire range of the formation voltages (0–10 V vs SCE). The outermost region consists entirely of ^{16}O, and the ^{18}O region is always adjacent to the Ti metal. The two distinct structures observed can be consistent with both the point defect model (PDM) or high-field model (HFM), assuming the mobility of titanium cations is much higher compared to the mobility of oxygen ions. No Ti or ^{18}O loss into the electrolyte during anodization is detected. Linear growth rate is observed in 0–10 V range vs SCE with experimental anodization ratio of 24.5±0.6 Å V^{-1}. Mott–Schottky (MS) analyses show positive slopes, indicating formation of an *n*-type TiO_2 semiconductor, with O vacancies (or Ti interstitials) as major charge carriers in the 0–10 V range. Charge carrier densities, $N_D = (0.8\text{-}5.0)\times10^{21}$ cm^{-3} were calculated from Mott–Schottky analysis and were well within the range of results reported in the literature. We observe derease in the charge carrier densities above ~4 V vs SCE, that can be connected to defects annihilation or minor modification in the structure of the growing TiO_2 film.

1. Introduction

Titanium (Ti) is ubiquitous in many applications, including biomedical implants. Ti has the highest ratio of strength to weight among common metals, high melting temperature (T_m=1673 K), and good corrosion resistance under ambient conditions. This stability is due to the formation of a passive TiO_2 layer, initially only ~ 2–4 nm thick, which protects the bulk Ti metal from further oxidation [1]. The oxide is thermodynamically stable, so few adverse reactions occur on the surface of the oxide. However, many factors can impact this process: composition, structure, roughness, and the specific tissue or liquid environment [2]. Electrochemically formed oxide films on Ti can be amorphous or crystalline, depending on the final anodic potential and electrolyte involved. This can directly affect the biocompatibility of Ti, as thickness and crystallinity (e.g., rutile vs. anatase) can affect the degree of adsorption from human plasma: i.e., rutile has closer packed structure with less ion diffusion compared to anatase. Ti oxide films with anatase and/or rutile crystal structure showed excellent apatite-forming ability,

compared to amorphous films, which is a prerequisite for biocompatibility [3].

Important properties relating to the TiO_2 layer can be controlled during anodic oxide growth, including morphology, surface roughness, and crystal structure [4,5]. The parameters of electrochemical anodization that can be used to control these factors include electrolyte composition, temperature, current density, anodization time and anodization voltage [6–8]. The different crystalline phases that can be obtained are rutile (tetragonal), anatase (tetragonal), and brookite (orthorhombic), with the anatase being metastable, and rutile having the highest chemical stability [9]. In this study, TiO_2 layers have been anodized using constant temperature (*T*=293 K), electrolyte composition (0.27 M NaCl), anodization time (*t*=6 h), and voltage in the 0–10 V vs SCE range. This allows films to be grown under controlled steady-state current conditions in order to achieve desired properties and examine the atomistic growth model. Electrochemical oxidation models typically involve descriptions of each ionic species present, and their associated transport mechanisms through an existing oxide. It is

generally accepted that the rate of anodization is limited by the mass-transport of ionic species through a pre-existing oxide film. Two major models have been developed in the past to describe anodic oxide growth based on this ionic mass-transport: the high-field model (HFM) and the point defect model (PDM) [10]. Both models pertinent to our study are described briefly below.

According to the HFM, in the presence of strong electric fields ($\sim 10^9$ V/cm), oxide formation kinetics is dependent on the migration of the ions through the oxide film [11]. Günthershultze and Betz in 1934 described the kinetics of oxide growth in terms of ionic current density being an exponential function of the electric field within the film [12]. Verway expanded this in 1935 and included the concept of jump distances between lattice sites, and the required activation energy for jumps between these sites [13]. Later, Cabrera and Mott further elaborated on the formalism by the addition of the frequency of atomic vibrations [14]. They also suggest it is the injection of cations into the oxide, across an activation barrier at the metal/oxide interface. In terms of charge carriers, Günthershultze and Betz [12] used both cations and anions in their description. Mott and Cabrera [14] and Verwey [13] described only the contribution of metal cation interstitials. Now, it is well established that for most so called valve metals (Ta, Al, Nb, Ti, etc.) both cations and anions contribute to oxide growth [10]. Fig. 1 gives a schematic representation of the HFM at the molecular level, note that charged defects can behave similarly to vacancies or interstitials; and they can migrate with and without exchange with the oxide lattice. Cations are driven down the potential gradients, migrating from the metal/oxide interface towards the oxide/solution interface where they react with oxygen in the electrolyte. Likewise, anions are transported from the oxide/electrolyte interface to the metal/oxide interface, where they react with the metal. If both metal cations and oxygen anions are mobile within the oxide, new oxide growth will happen at both the oxide/electrolyte and the metal/oxide interfaces simultaneously, with the relative contribution of each being a function of the metal and processing conditions [15].

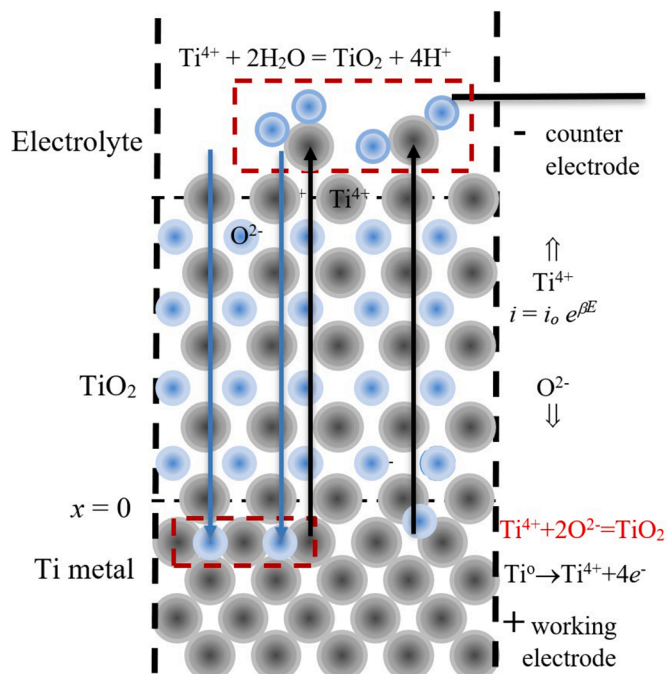While within high-field models, there is a variety of views about whether charged defects behave as vacancies or interstitials; and whether or not they exchange with the oxide lattice, the important characteristic of HFM is exponential ion current-field relation found during anodizing. The quantities t_a and t_c are the anionic and cationic transport numbers respectively which represent the fraction of newly formed oxide due to that ion, and reflect the relative ionic mobilities. The sum of the contributions from each ionic species must be: $t_a + t_c = 1$ [16].

One of the propositions of the point defect model (PDM) is that the magnitude of the electric field through the oxide is independent of applied voltage because of buffering effects (i.e., Esaki tunneling) [17], and so a "low-field" approach can be considered, because the effective field through the oxide films is low enough that the Nerst–Einstein and generalized Fick's law describe the ionic transport [10]. A bi-layer structure is postulated, as illustrated in Fig. 2, with an initial passive oxide (or sulfide, hydride, etc.) called the "barrier layer" which is adjacent to the metal surface and which has a high concentration of point-defects that carry the ionic current with negligible interaction between point defects [18,19], and a "precipitated" outer layer that forms over time between the solution and barrier layer [19]. Anion vacancies are created at the metal/oxide interface and transported to the oxide/electrolyte interface where they are consumed. Likewise, cation vacancies are created at the oxide/electrolyte interface and transported to the metal/oxide interface where they are consumed. The latter process results in either metal cation dissolution into the electrolyte or the precipitation of a new oxide [10]. An important consequence of this is that according to the PDM, the oxygen atoms which composed the barrier layer should remain in the barrier layer, as the oxide growth progresses into the metal (representing the "corrosion front"), while the precipitated outer layer grows *via* the incorporation of O from the

Fig. 1. A schematic representation of the HFM's description of ion transport. The largest potential drop between anode and cathode occurs within the existing oxide and this drives cation and anion transport and thus oxide growth. These charged defects can behave similarly to vacancies or interstitials; and they can migrate with or without exchange with the oxide structure.
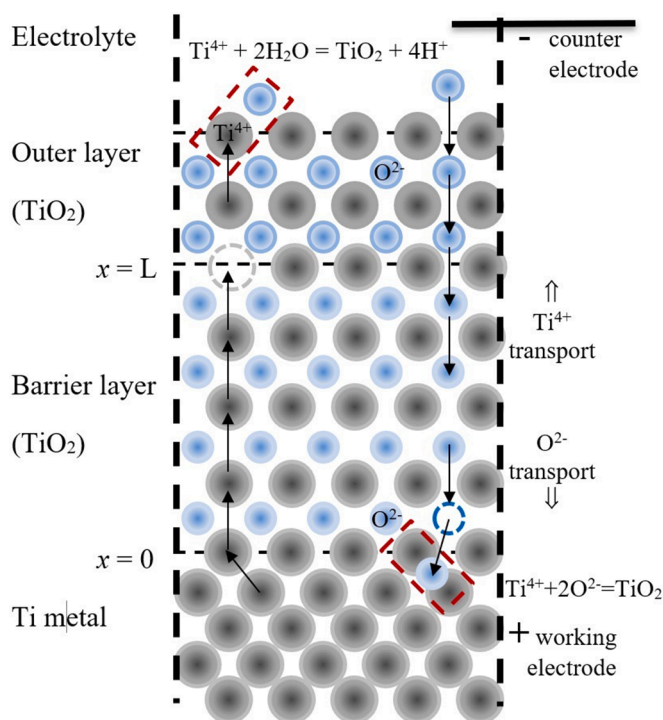

Fig. 2. A schematic representation of the PDM. In the PDM, the original highly defective oxide is referred to as the barrier layer. The grey spheres represent Ti atoms, and the blue spheres represent O atoms, while the dashed spheres represent the respective vacancies in the oxide. The series of arrows depicts the successive movement of the ionic species, which results from repeated fillings of the vacancy and its subsequent annihilation at the appropriate interface. The barrier layer grows into the metal while the outer layer forms by reaction of the Ti cations with water.

electrolyte. In many of studies, using PDM as an assumption, it is found that the doubly charged oxygen vacancies V_o in titanium oxide, dominate over the metal interstitials, e.g. Ti_i^{x+}, and cation vacancy V_{Ti} [5,20].

The anodization of Ti has been studied extensively by use of electrochemical techniques, from which inferences are made about the electrode structure [21]. The electrode composition is rarely quantified directly *via* high-resolution elemental depth profiling. The studies that discuss compositional differences in terms of the predictions of the PDM and HFM are also rare [22]. Occasionally, techniques like Auger electron spectroscopy (AES), secondary ion mass spectrometry (SIMS), and X-ray photoelectron spectroscopy (XPS) are used for anodic oxide characterization, but often it's not taken into account that each theory predicts different oxide "phases", for example the PDM predicts that the "precipitated" outer layer might be 10^2–10^3 times as thick as the barrier layer [23].

Khalil and Leach imbedded Rn^{222} atoms just below the surface of Ti metal, to act as Kirkendall markers [16], and measured the energy distribution of emitted α particles before and after anodization. The α particles are required to travel through newly grown oxide, losing energy with the well-known stopping powers. The thicker the oxide layer is the more energy loss α particles would experience. If only anions are mobile, the α particles markers would be in the same relative position and the oxide growth would proceed from the metal surface inwards. If only cations are mobile then the markers would be buried under the full thickness of oxide. The authors concluded that the 33% of the oxide growth was due to cation transport while the remaining 67% of oxide growth was a consequence of the O^{2-} mobility. This result is consistent with both the PDM and HFM as both describe oxide growth in terms of the relative flux of cations and anions.

Tun et al. used *in-situ* neutron reflectometry to study the effect of Ti anodization in aqueous NaCl with a pre-existing passive air-grown oxide [22]. During post-anodization analysis they found that the oxide was composed of two distinct regions: an outer region that contained a lot of hydrogen, probably from OH^- ions in the electrolyte being incorporated into the oxide, and the second inner region with the same thickness and composition as the original passive oxide. Such a bi-layer structure led to the authors choosing the PDM as the preferred growth model. The authors note that their results were also consistent with OH^- being stripped of hydrogen by the large potentials in the film (according to the HFM) while the oxygen ions passes through the oxide and reacts with Ti. However, they found that the H-free region is the exact same thickness as the air-grown oxide, which would be a necessity according to the PDM.

Oxygen (^{16}O/^{17}O/^{18}O) isotopic labeling is a well-established procedure to measure the transport and reaction mechanisms of the high-temperature oxidation of metals [24–26]. In this work, two ion-beam depth profiling techniques known as medium energy ion scattering (MEIS) and nuclear reaction profiling (NRP) were used to characterize the electrochemically formed titanium oxides that result from the isotopic labeling procedure described above. MEIS involves the analysis of the energy-distribution of backscattered ions, and results in quantitative elemental areal densities as functions of depth. In MEIS, incident H^+ will backscatter off the O isotopes of interest but also the Ti, Si, and any other elements present whose signal may obscure the O features. NRA can be performed using a reaction that is only sensitive to ^{18}O, and provides a second complementary approach to depth profiling the anodic oxides. Electrochemical impedance spectroscopy (EIS) involves applying an AC potential to a system and analyzing the resistance and reactance (impedance) of the system [27]. By relating the complex phase change and electrical impedance magnitude to the applied frequency, a Bode plot can be constructed [28], providing the information about the number of layers in a structure, and, by fitting the data to an equivalent electrochemical circuit, properties such as resistance, and capacitance of individual elements of the system may be calculated [29].

2. Experimental details

To characterize Ti anodization at the atomic level, O isotopic labelling was used in conjunction with high-resolution ion-beam depth profiling techniques and electrochemical impedance spectroscopy (EIS). Ultra-thin Ti films were deposited onto Si(001) substrates using magnetron sputter deposition, and prior to exposing them to ambient conditions, Ti films were exposed to $H_2^{18}O$ vapours, to form a passive oxide consisting of only $Ti^{18}O_2$. After this, the films were anodized in $D_2^{16}O$ in the 0–10 V vs SCE range. The concentration of each O isotope as a function of depth can support a given anodization model. For example, if the ^{18}O region is the same thickness as the original passive oxide and is located at the metal/oxide interface, representing the corrosion front (i. e., $Ti^{16}O_2$/$Ti^{18}O_2$/Ti/Si(001)), this is evidence of the PDM mechanism. In the HFM, the original oxide acts as a passive medium through which ions pass and the model predicts that the $Ti^{18}O_2$ region will be situated between two newly-formed $Ti^{16}O_2$ regions, the thickness of each dependent on the mobility of the respective ion. There are three possibilities under assumption of HFM. (i) If Ti cations and O ions have comparable mobilitites, $Ti^{16}O_2$/$Ti^{18}O_2$/$Ti^{16}O_2$/Ti/Si(001) layered stucture will be obtained; (ii) if the mobility of Ti cations is much higher compared to the mobility of O ions, new $Ti^{16}O_2$ forms on the outer surface resulting in the $Ti^{16}O_2$/$Ti^{18}O_2$/Ti/Si(001) structure; (iii) if the mobility of O ions is higher compared to Ti cations; new $Ti^{16}O_2$ layer forms at the interface, giving $Ti^{18}O_2$/$Ti^{16}O_2$/Ti/Si(001)) structure.

2.1. Depth profiling samples and isotopic labeling

The depth profiled samples were created by depositing Ti films with physical thickness of 14.0±0.5 nm, by magnetron sputtering onto Si (001) 4.5" wafers. The Ti films were exposed to isotopic ^{18}O water *in-situ* to form ultra-thin TiO_2 films. Uniformity of the Ti film composition and thickness (±4%) was confirmed by X-ray reflectometry (XRR) and Rutherford backscattering spectrometry (RBS). Under ambient conditions, the $Ti^{18}O_2$/Ti/Si(001) films were anodized in $D_2^{16}O$ water over a range of voltages of 0–10 V, measured in potentiostatic mode, resulting in ~4–30 nm oxide regions. More details on anodization conditions are provided below.

2.2. Anodization of samples for electrochemical impedance spectroscopy (EIS)

Anodization experiments were conducted at pH 7, 0.27 M NaCl in type 1 18.2 MΩ cm^{-1} water, at constant voltage in a 3-chambered electrochemical cell. ASTM Grade-2 Ti was submerged in an electrolyte consisting of 0.27 M NaCl in 18.2 MΩ (Type 1 – Ultrapure) water, with a Pt-mesh counter electrode, and a saturated calomel reference electrode (SCE). Prior to anodization, the Ti was polished using a P1200 silicon carbide polishing paper with Type 1 Ultrapure water, and dried using an argon stream. During anodization, Ti was submerged in the electrolyte, and the open circuit potential (OCP) was measured until OCP stabilized at less than 10 mV/min difference. A potential (forming potential) of between 1 and 10 V (vs SCE) was applied, for a total of 6 hours, until the current stabilized at ±0.01 (A/cm^2)/min.

Crevice corrosion of Ti can be influenced by many factors including temperature, solution chemistry and pH, alloy composition, and metal potential. For instance, crevice corrosion resistance of Ti alloys decreases with increasing temperature, with a threshold, around 60–65 °C, for the initiation of crevice corrosion [30,31]. To the best of our knowledge, there was no localized corrosion issues at our anodization and EIS condition at room temperature, the microscale morphology was viewed before and after anodization, both before EIS and after EIS, with no noticeable morphology changes under scanning electron microscopy analysis.

2.3. MEIS setup

The thickness and composition of the isotopically labelled TiO_2 films were measured by MEIS, using 200 keV H^+ ions to maximize the separation between the ^{18}O and ^{16}O peaks. In this energy range, the energy loss experienced by protons as they penetrate the medium under investigation is maximized, providing the greatest depth resolution.

MEIS was performed in "double-alignment" geometry, at the Western University Tandetron Accelerator Facility, using a toroidal electrostatic energy analyser (HVEE). The incident beam was aligned along a major crystallographic direction of the Si(001) substrate (i.e., channeling), and the center of the toroidal electrostatic energy analyser (TEA) was aligned to another crystallographic direction (i.e., blocking). This produced a significant reduction in backscattering intensity from the Si substrate, preventing the Si spectral feature from obscuring lighter elements (i.e., the O isotopes) [32,33]. The details of the experimental apparatus and MEIS image corrections can be found in Kim et al. [34]. The experimental MEIS spectra were fitted using MEISwin v.1.05 software [35]. The backscattering intensity has been summed over a 1° angular range for improved statistics.

2.4. NRP setup

The areal density of ^{18}O in the oxide films was also measured with nuclear reaction profiling *via* the narrow $^{18}O(p,\alpha)^{15}N$ resonance ($\Gamma\sim100$ eV), appearing on the H^+ cross-section curve at 151 keV. The oxide films were bombarded with a proton beam (produced at the Western University Tandetron Accelerator Facility) and the ejected α particles in the 3–4 MeV range [36] were measured by a Si surface barrier detector. The proton beam impinged onto the samples at normal incidence. A $Ta_2^{18}O_5$ calibration standard with known ^{18}O areal density was used for ^{18}O quantification. To avoid detection of backscattered protons from the target, an aluminized polyethylene terephthalate (Mylar®) absorbing foil was positioned in front of the detector.

2.5. ERD setup

Areal densities of hydrogen and deuterium were measured with elastic recoil detection (ERD). Samples were probed using a 2.9 MeV ^{4}He beam in a conventional ERD setup with incident angle of 75°, recoil angle of 30° in IBM geometry, and 12.2 mm Al-coated Mylar range foil. Kapton and H-implanted Si targets were used as standards to determine the detector solid angle (both were within 3% of each other).

2.6. EIS setup

Mott–Schottky (MS) analysis was used to probe the interfacial properties of the oxide films. The capacitance of the Ti oxide was measured using electrochemical impedance spectroscopy (EIS), during which a bias was applied in 0.05 V increments, from the open circuit potential (OCP) to ±1 V vs OCP, while successive impedance measurements were taken. The magnitude and phase shift of the AC current being applied during impedance measurements gives information on the interface, which is described using an equivalent electrochemical circuit (EEC), i.e., the properties of a material are defined using generic circuit components that would yield the same electrical response produced by the electrochemical cell. Using Zplot software, numerical values for the relative strengths of each of the components of the EEC can be simulated, and values of material resistance R (Ω cm^2), interface capacitance C, (nF cm^{-2}) were inferred.

EIS measurements were taken on the anodized Ti, which was coated in epoxy such that a 0.73 cm^2 area was exposed, and edge effects were minimized. The measurments employed a three-chambered electrochemical cell, with a 0.27 M NaCl in 18.2 MΩ (Type 1 – Ultrapure) water electrolyte. The reference electrode was a saturated calomel electrode, and the counter electrode was a Pt-sheet. Impedance measurements were taken over a range of 10 mHz to 1 kHz, using a combined Modulab frequency response analyzer (FRA) and potentiostat.

2.7. XPS and XRD

The oxidation states of Ti in the TiO_2 films were analyzed by XPS (Surface Science Western) using a monochromatic Al Kα source (Kratos AXIS Ultra Spectrometer). The XPS energy was calibrated by assigning the C 1s feature (C-C bond of adventitious carbon) at 284.6 eV. Simulated photoelectron spectra were calculated using CasaXPS software [37]. The crystallinity of the films was assessed with X-ray diffraction (XRD) using a Cu Kα source (Rigaku SmartLab 2D with HyPix-3000 detector Diffractometer).

3. Results and discussion

MEIS was used to estimate film composition and thickness. Fig. 3 shows the compositional changes of the anodic Ti oxide, as a function of anodization voltage. These structural changes are reflected in the differences between the H^+ backscattering spectra of the $Ti^{18}O_2/Ti/Si$ (001) films acquired before (as is) and after anodization (2 and 5 V), in $D_2^{16}O$. The MEIS spectra were taken using 200 keV H^+, with an incident angle of $45°$, and a scattering angle of $135°$.

From the MEIS spectra in Fig. 3 one can observe that incident ions that scatter from heavier elements will be detected at higher energies, leading to target elements appearing in order of decreasing mass (with Ti being the heaviest). The H^+ energies corresponding to the high-energy edges of Ti, O, and C (but not Si) peaks are in good agreement with the binary collision model, which means these elements are located on the surface of the films, while Si is entirely buried by the films. The film surfaces contain a small amount of hydrocarbon contamination, confirmed from a minor C surface peak (also measured by XPS).

MEIS backscattering yields are linearly proportional to a given elemental areal density. In Fig. 3, the lower areal density of Ti in the oxide results in a decrease in peak intensity, relative to metallic Ti and
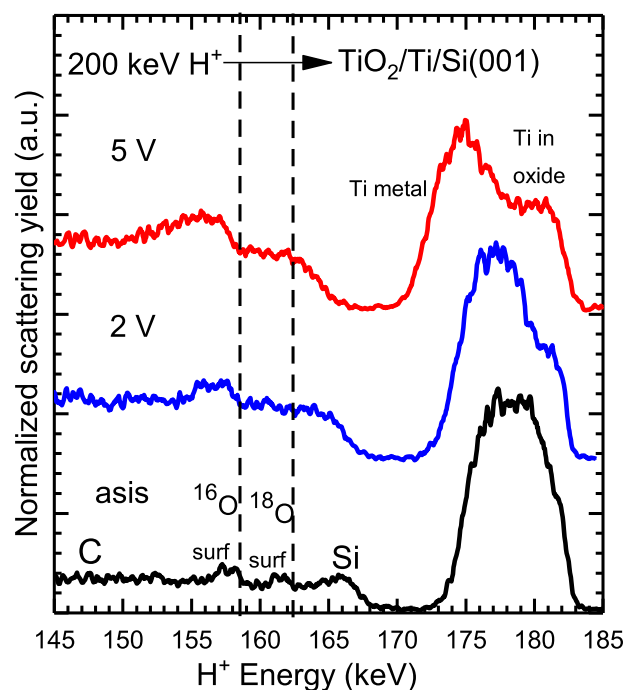

Fig. 3. The MEIS spectra for $TiO_2/Ti/Si(001)$, before (as is $\equiv$ as prepared) and after (2 and 5 V) anodization. Differences in anodic oxide composition are reflected in the spectra. Data were acquired using a beam of 200 keV H^+ with an incident angle of $45°$, and a scattering angle of $135°$.

reflects the stoichiometry of Ti in the oxide. Also, incident H^+ ions inelastically lose energy from electronic interactions as they penetrate the target. The greater the oxide thickness, the greater the energy loss before backscattering from the Ti metal. So, an increase in oxide thickness corresponds to the broadening of the Ti peak to lower energies. The position of the Ti peak is pushed to lower energies by ≈ 3.4 keV in the set of samples from as-is to 5 V anodized. Simultaneously, as Ti metal is consumed, the metallic Ti peak becomes increasingly thinner. No changes are observed in the total areal density of Ti, within experimental uncertainty $(4.47\pm0.07)\times10^{16}$ atoms/cm^2 (summed over the TiO$_2$ and Ti layers), indicating no Ti is lost to dissolution into the electrolyte during anodization.

The surface positions of the ^{18}O and ^{16}O peaks are provided by the vertical dashed lines in Fig. 3. From as-is sample to 2 V anodization, the ^{18}O peak position moves to lower energies by 1 keV and by another 2.6 keV from 2 V to 5 V anodization, until it overlaps with the ^{16}O surface peak. This energy loss implies that the oxide layer which contains ^{18}O is covered by an increasingly thickening layer oxide containing ^{16}O. The lack of change in the ^{16}O surface position relative to its position for as-is sample suggests that ^{16}O consistently composes the outermost oxide layer. From as-is to 5 V, the ^{16}O peak width increases monotonically, implying that a majority of the oxide growth is driven by an increasing incorporation of ^{16}O. The procedure for determination of oxygen depth profiles relies on detection of ^{18}O and ^{16}O surface peak positions and the energy loss though the film, ΔE. The statistical uncertainties on ^{18}O and ^{16}O peaks were between 10% and 15%, depending on the thickness. Another two factors contributing to the MEIS depth profiles are Ti peak and the Si edge position, as described above. Detailed discussion of uncertainty analysis for MEIS from energy spectra is given in details elsewhere [38]. Due to the ^{16}O and ^{18}O peaks overlapping at higher anodization voltages, more accurate ^{18}O depth profiling was produced using NRA.

XPS was performed to provide insights into the chemcal composition of the films, and to justify the stoichiometry of the oxide used in the MEIS simulations. The high-resolution XPS spectrum for the Ti 2p region is presented in Fig. 4. The main doublet peak (459.0 eV and 464.5 eV [39]) attributed to Ti(IV), is evidence that TiO$_2$ is the primary constituent of the oxide ($\s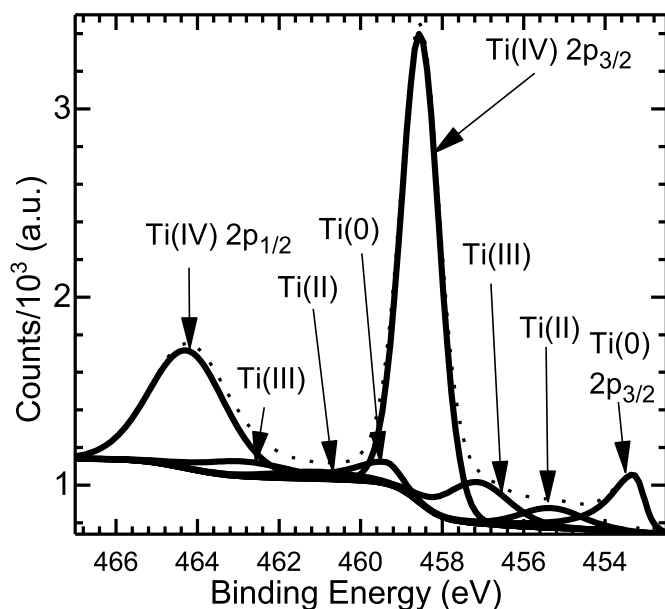im 85\%$ in the oxidation state Ti(IV)). The peaks can be de-convoluted into a number of minor contributions from trace amounts of other oxides: TiO, for which the binding energy for the 2p$_{3/2}$ peak is $\sim$ 454.6 eV and the 2p$_{1/2}$ peak is found at $\sim$ 460.2 eV [40]; and Ti$_2$O$_3$, for which the binding energy is $\sim$ 456.8 eV for the 2p$_{3/2}$ peak and $\sim$ 462.0 eV 2p$_{1/2}$ peaks [40]. There is evidence of a metallic Ti 2p$_{3/2}$ peak at 454.0 eV [41], even after anodization to 2 V the metallic Ti film is not completely converted to oxide, and TiO$_2$ is still thin enough that metallic Ti photoelectrons can be detected. Wang et al. noted that 90% of their anodic Ti oxide, for the first 2.5 nm was TiO$_2$ (a thickness comparable to ours), with an increase in sub-oxides (TiO and Ti$_2$O$_3$) occurring at greater depths into the film below 2.5 nm [42].

MEIS spectra were simulated to match the experimental spectra in order to provide quantitative information on film thickness and elemental areal density. This was done by constructing a series of layers and controlling their elemental composition and thickness. These values were modified until the simulated results matched the experimental energy spectrum. The simulated O depth profiles that show the effect of anodization of Ti^{18}O$_2$/Ti/Si(001) in D$_2^{16}$O, on the ^{18}O and ^{16}O depth distribution, are shown in Fig. 5 for the anodization voltages from as-is to 1.5 V (a, c) and 2 – 10 V (b, d), respectively.

Fig. 5 clarifies some of the trends shown in Fig. 3, in that it depicts the total ^{16}O region thickness increasing monotonically as a function of anodization voltage, while its surface position is maintained. Ultimately, a Ti^{16}O$_2$/Ti^{18}O$_2$ bi-layer structure is maintained with the Ti^{18}O$_2$ regions representing the corrosion front adjacent to the un-oxidized metal and the Ti^{16}O$_2$ oxide region consistently adjacent to the oxide/electrolyte interface.

It was observed from the MEIS spectra that for samples anodized at higher voltages (e.g., the 5 V sample, in Fig. 3), the ^{16}O and ^{18}O peaks overlap, which complicates analysis of these data. For this reason, NRP was chosen as a complementary method of depth profiling ^{18}O, as it is reaction-specific and only sensitive to ^{18}O (no signal from ^{16}O, the Si substrate, etc.). The ^{18}O depth profiles measured with the 151 keV ^{18}O (p,α)^{15}N resonance are summarized in Fig. 6.

The trends observed from MEIS are consistent with those from NRP (Fig. 6), being summarized by the anodic films maintaining a bi-layer structure, where ^{18}O-containing oxide is adjacent to the Ti metal, and oxide regions closer to the surface are composed entirely of Ti^{16}O$_2$. Note that the resonance is only sensitive to ^{18}O, so ^{16}O cannot be measured directly. The position of ^{16}O between the film surface and the Ti^{18}O$_2$ region is implied from the energy loss in a layer with no ^{18}O present because there is no α emission from the surface using 151 keV H$^+$. Emission only occurs when the incident beam energy is increased so that the H$^+$ ions penetrating the ^{16}O regions have lost precisely enough energy that the resonance energy of exactly 151 keV is reached. The energy loss specific to H$^+$ in TiO$_2$ is known as its stopping power [36,38].

Fig. 7(a) shows the linear relationship between anodization potential and oxide thickness as derived from MEIS, using TiO$_2$ bulk densities. The slope of the linear fit line is often known as the "anodization ratio" that is given here as 24.5±0.6 ÅV^{-1}, consistent with work by others [16,22]. Titanium oxide thickness extrapolated to 0 V is 6 nm, also consistent with work by others. Fig. 7(b) presents O^{16} and ^{18}O areal densities as functions of anodization voltage derived from MEIS and NRP and the total ^{16}O areal density derived from MEIS.

No ^{18}O is lost to the liquid phase because its areal density remains constant across all anodization potentials within experimental uncertainty (Fig. 7b), with an average value of $(1.29\pm0.06)\times10^{16}$ atoms cm^{-2}. Since the ^{18}O areal density remains constant the linear increase in oxide thickness (Fig. 7) implies that growth proceeds by the increasing incorporation of ^{16}O (this is confirmed by MEIS).

Fig. 8(a) shows a typical open circuit potential (OCP) measured for the sample prepared at anodization voltage of 2 V. OCP was monitored until the rate of change of voltage reached 10 (mV)/minute. OCP curves for samples produced at different anodization voltages (in the 1.0–7.5 V range) follow the same trend. Steady-state current densities for various anodization potentials are shown in Fig. 8(b), with the average current
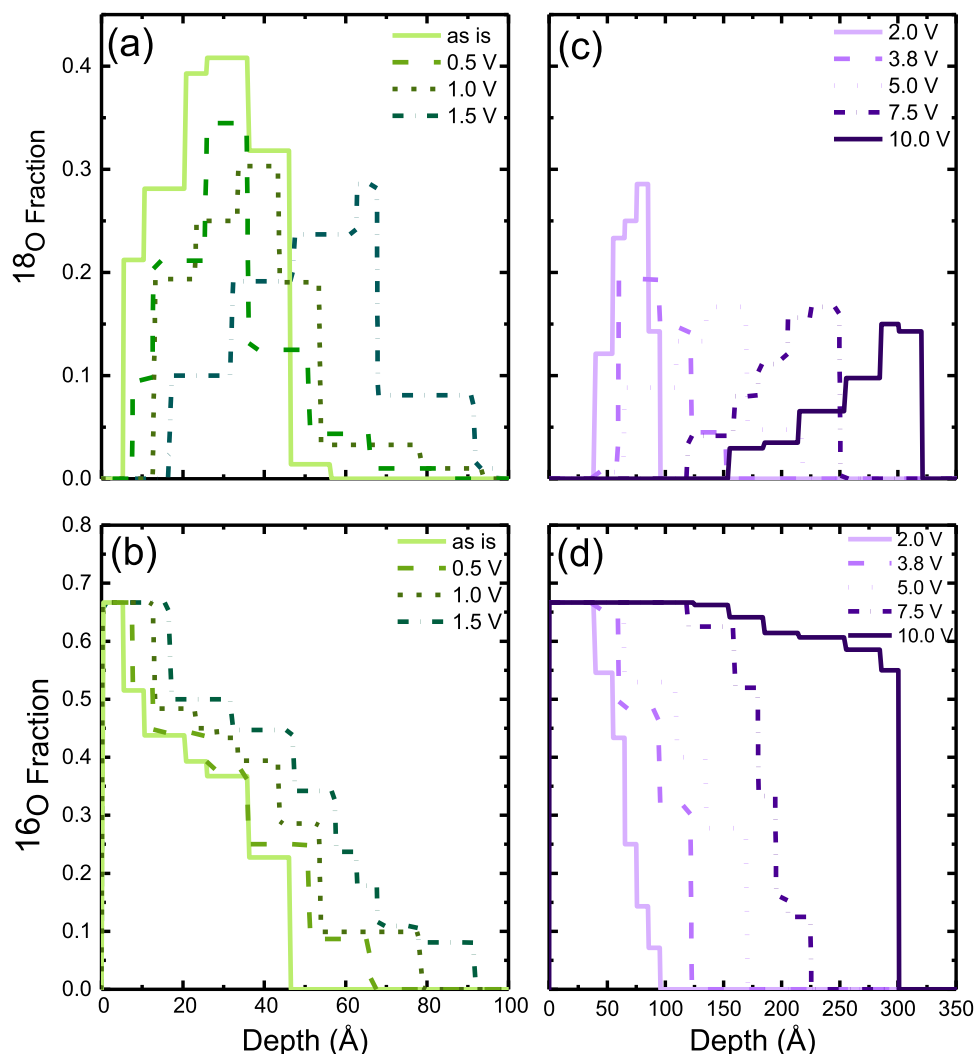

Fig. 4. XPS data for the Ti *2p* region, showing the oxidation states of Ti. The spectrum corresponds to the TiO$_2$/Ti/Si(001) sample that was anodized at 2 V in D$_2^{16}$O. Experimental spectrum is shown by a dashed line, XPS spectra peak fits for different oxidation states of titanium are shown by solid lines.

Fig. 5. The evolution of the MEIS ^{18}O ((a) and (c)) and ^{16}O ((b) and (d)) depth profiles, after anodization in $D_2^{16}O$, from as prepared (as is) to voltages up to 10 V. Depth profiles are derived from simulations of the MEIS spectra and show the fraction of the respective isotope in the oxide. To summarize the effect of anodization on the O profiles; a $Ti^{16}O_2/ Ti^{18}O_{2-x}^{16}O_x$ bi-layer structure is maintained over all voltages.

densities from the different day runs, and standard deviations shown as error bars. Note that lower anodization voltages resulted in lower steady-state current density (in the 1.0–2.0 μA/cm² range for 1–3.8 V), the steady state current densities increase for samples anodized at 5 V and 7.5 V.

EIS spectra in Nyquist and Bode formats, Fig. 9 (a) and (b), present high corrosion resistance in 0.27 M NaCl solution, with impedance values approaching 10^6 Ω*cm² at frequencies below 10 mHz. The impedance can be fitted with good precision using a two time-constant circuit shown as inset in Fig. 9 (b), however, the fit is not perfect. This two-time constant circuit includes solution resistance (R_S), circuit elements associated with the growing Ti oxide films (constant phase elements (CPE) and resistor representing impedance of the anodic film on Ti metal, CPE_Ox and R_Ox) and oxide defects (CPE_df and R_df). The last elements will have constant component (R and C) associated with initial barrier layer, and non-constant components related to growing Ti oxide layer, and defects associated with it. A capacitive response with a phase angle close to -90° over a wide frequency range, is shown in Fig. 9 (c), indicating formation of a space-charge layer in the oxide. Our fitting results of impedance spectra for titanium oxide films are summarized in Table 1. Note that solution resistance (R_S) and defect resistance (R_df) are almost constant, while oxide resistance and constant phase element component of oxide and defects are changing significantly with

anodizing voltage.

Mott–Schottky plots uses the reciprocal of the square of effective capacitance of the system (C_{eff}) calculated using the equivalent electrochemical circuit (Fig. 9b) ($1/C_{eff}^2$) versus the potential difference between bulk semiconductor and bulk electrolyte (V). Analysis of MS plots (MSA) allow us to determine donor densities (N_D) and the flat band potential (E_{FB}) from Eq. (1) [43]:

$$\frac{1}{C^2} = \frac{\pm 2}{\varepsilon \varepsilon_o e N_D} \left(E - E_{FB} - \frac{k_b T}{e} \right) \tag{1}$$

where, $e, \varepsilon, \varepsilon_o$ stands for the electron charge, the dielectric constant, the permittivity of a vacuum, and k_B and T denote the Boltzmann constant and absolute temperature (300 K), respectively. MS dependences were measured for samples anodized at voltages in 1–10 V range, and Fig. 10 shows a representative Mott–Schottky graph for a pure Ti specimen anodized at 7.5 V, with several regions defined. There is a linear relationship between C^{-2} and V over a range of potentials indicating semiconducting behaviour. When potential is applied between semiconductor and electrolyte, it raises the Fermi level of electrons; consequently, the capacitance increases, and the reciprocal square capacitance decreases forming a linear part of Mott–Schottky plot. The positive slope of this region can be attributed to an n-type semiconductor behaviour. While the relationship observed at a higher
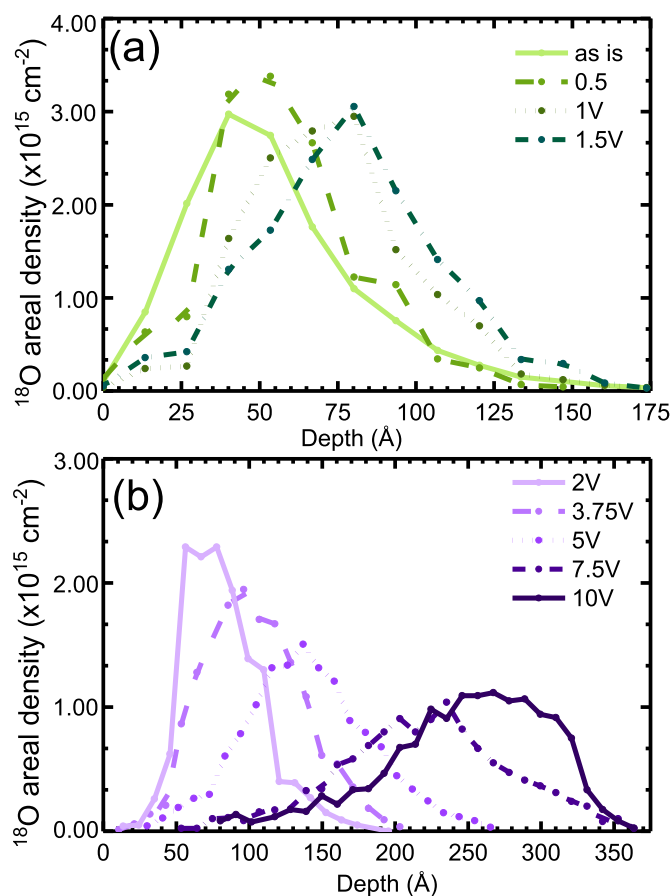
Fig. 6. Nuclear reaction profiling data for the anodization voltages from (a) "as is" to 1.5 V and (b) 2–10 V. Conversion of the energy scale into a depth scale is done by using the known H^+ energy loss in Ti oxide, and conversion of counts into ^{18}O concentration is done through the use of a ^{18}O standard.

potential range indicates dielectric (non-semiconductor) behaviour. For instance, at higher potentials the Fermi level reaches the bandgap state level or goes above, capacitor is discharged, and a plateau occurs depending on the value of the capacitance of Helmholtz layer at the electrolyte side.

The flat band potential can be estimated from Mott–Schottky plots by extrapolating semiconductor region and taking the absolute value of the potential at the X-axis intercept. Flat band potentials estimated for Ti foil are presented as a function of anodization voltage in Fig. 11a. The Figure shows an increase of the flat band potential for oxides grown at <4 V (consistent with the values reported by Ansari and Fattah-Alhosseini [43]) and the flat band potential achieves a constant value in oxide films grown at higher voltages. The doping density was calculated using Eq. (2),

$$\frac{d\left(C^{-2}\right)}{dV} = \frac{2}{eA^2 \varepsilon\, N_D(\omega)} \qquad (2)$$

with C being the capacitance of the system, e the elemental charge, A the surface area, ε the dielectric permittivity, N_D the doping density, and ω the distance separating the two plates of the capacitor. Using the known dielectric constant of titanium oxide in the amorphous phase the doping density of ionic defects can be determined quantitatively at each anodic growth thickness. We acknowledge that this is not the best approximation as dielectric constant may also change with the changes in the doping density.

Fig. 11 (b) presents an increase in the charge carrier density with increasing anodization potential over the anodization range of 0–4 V followed by its decrease in films anodized at higher voltages. The slope
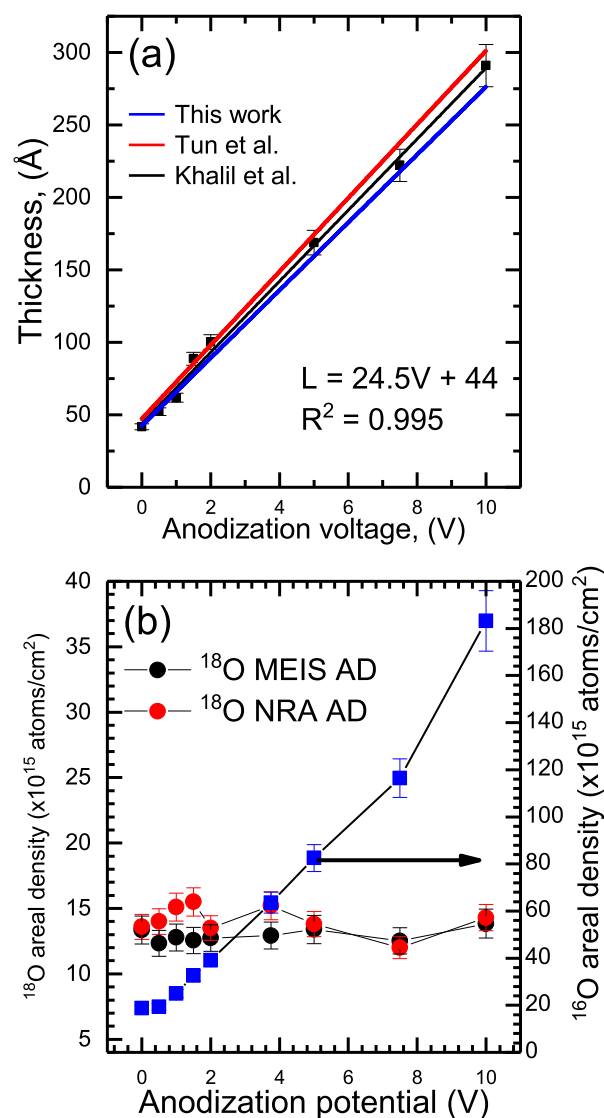

Fig. 7. (a) Growth of TiO_2 oxide as a function of anodization voltage. The blue line represents linear least squares fit. The red line is from [22] and the black line from [16]. (b) Variation in ^{16}O and ^{18}O areal density (AD) of the passive oxide as a function of anodization voltage. The areal density of ^{18}O from MEIS (black circles) is compared with the ^{18}O NRA (red circles) values.

of Mott–Schottky plot remains positive. At lower voltages, the *n*-type characteristics of the films are established by either O vacancies or Ti interstitials injected into oxide at the interface. This observed decrease in the charge carrier densities may represent a high-potential/ high-field annealing of defects in the oxide. As we noted below, the titanium oxides are definitely thicker when grown at higher potentials (2.5 nm/V) and there is some evidence in the literature that at potentials in the >4 V range the amorphous TiO_2 undergoes field-driven crystallization. Reduction in the charge carrier density leads to an increase in steady-state current as observed in this study for >4 V (Fig. 8b). The recorded values for N_D in the literature vary between 10^{18} and 10^{23} cm^{-3} [43, 44]; the exact value depends on the thickness of the oxide film, film crystallinity, and electrolyte. Our N_D values are in the $(0.8\text{-}5.0)\times10^{21}$ cm^{-3} range, comparable to the values reported by Ansari and Fattah-Alhosseini [43]. Yet, these carrier density values $((0.8\text{-}5.0)\times10^{21}$ cm$^{-3})$ are exceedingly high compared to the typical valeus for bulk n-type semiconductor $(\sim n\times10^{16}$ cm$^{-3})$ [45]. Consistent to our results, the oxygen vacancy concentration was found to exponentially decrease from 5.03×10^{20} to 3.91×10^{19} cm^{-3} as the film formation voltage was
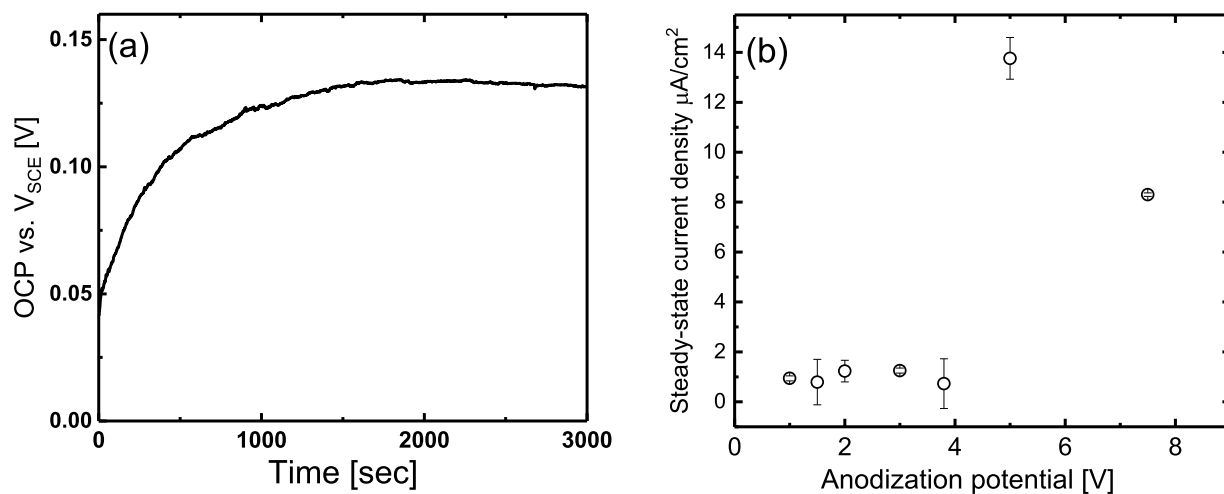
Fig. 8. (a) Open circuit potential (OCP), (b) steady state passive current density, A/cm^2, obtained during Ti anodization in 0.27 M NaCl solution at 21 °C. Average current densities are plotted with uncertainty bars showing the standard deviation for repeated measurements made under the same conditions on different days.
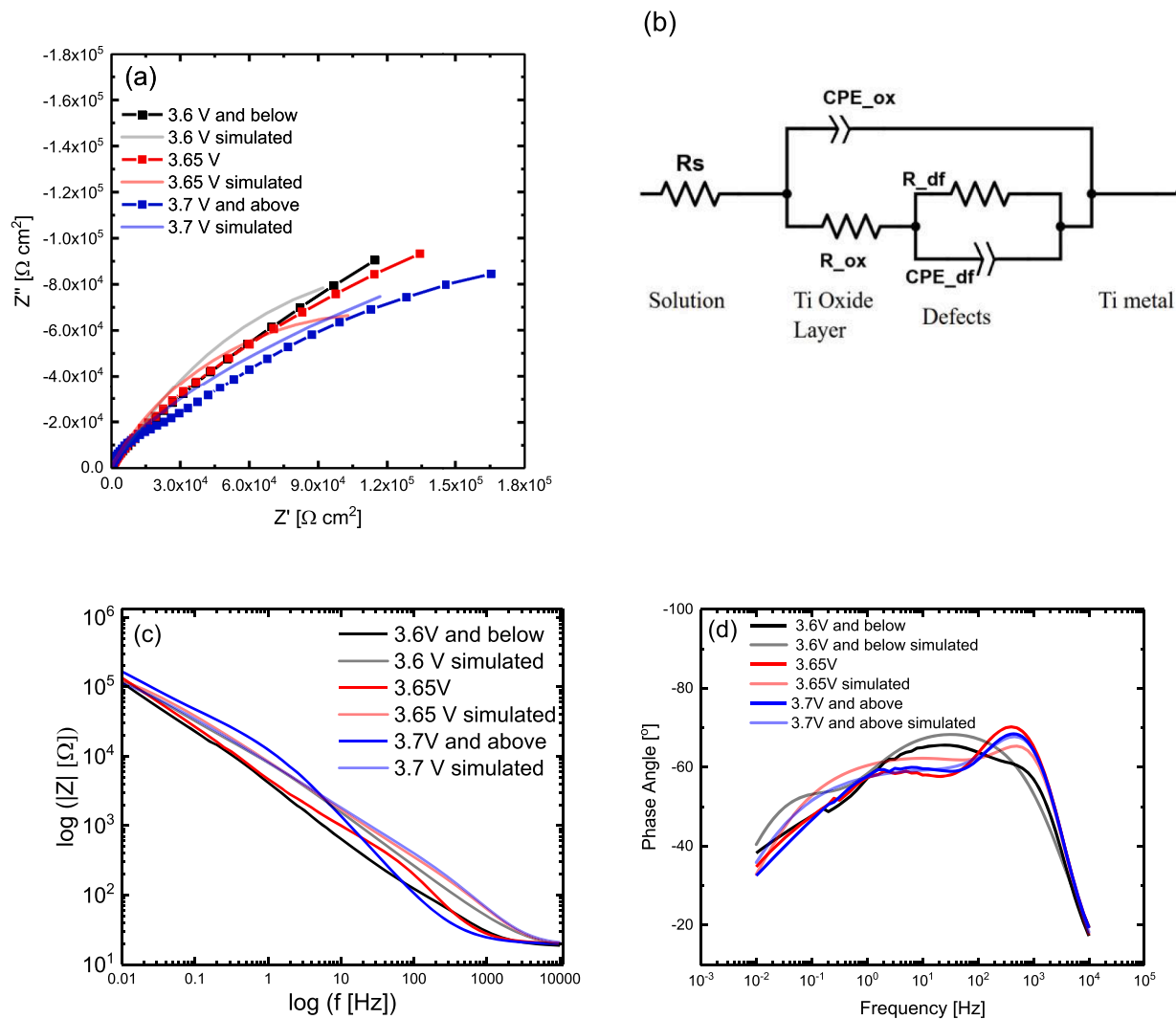

Fig. 9. (a) Nyquist plots with (b) the two-time constant equivalent circuit used for fitting including solution resistance (R_S), and circuit elements associated with the growing Ti oxide films (constant phase elements (CPE) and resistor representing impedance of the anodic film on Ti metal, CPE_Ox and R_Ox) and oxide defects (CPE_df and R_df); (c) and (d) Bode plots with simulated curves for the Ti film anodized at different voltages in NaCl solution at 21 °C. Note pronounced second time constant in the Bode plot when increasing anodization voltage higher than 3.65 V vs SCE.

Table 1
Fitting of impedance spectra for titanium oxide films.

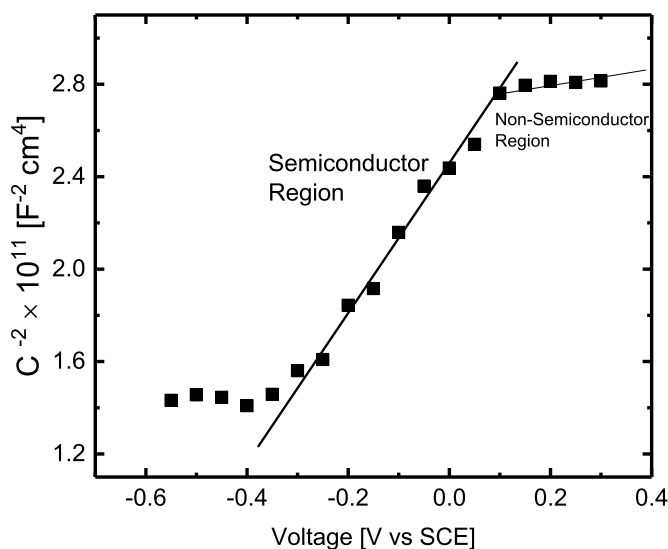| Fitting parameter	Anodization voltage, V		
	3.6	3.65	3.7
Rs, Ω	21.0	18.9	19.4
R_ox, Ω	239	296	430
Q_ox (F μF)	2.39×10^{-6}	3.05×10^{-6}	3.20×10^{-6}
α_ox ($0 < \alpha < 1$)	0.79	0.98	0.97
R_df, Ω	2.52×10^5	2.31×10^5	2.62×10^5
Q_df (F μF)	2.81×10^{-5}	3.05×10^{-5}	3.38×10^{-5}
α_df ($0 < \alpha < 1$)	0.68	0.65	0.62

Fig. 10. Mott–Schottky plot for an ASTM Grade-2 Ti sample that was anodized in 0.27 M NaCl solution at 7.5 V.

increased from 2.24 to 10.24 V for anodic titanium oxide film on Ti in 0.5 M H_2SO_4 [20].

Elastic recoil detection (ERD) spectra provide no evidence of deuterium (D) incorporation in the TiO_2 layer. It should be noted that our ERD setup has a detection sensitivity of approximately 10 ppm (by number of atoms) [36] and, therefore, it is possible that some undetected H or D remained in the film.

Our grazing angle XRD data (see Supporting Information, Fig. S1) shows no evidence of anatase or rutile phases within the limits of detection by the XRD instrument and technique used for this study that is aimed at crystalline phases. Marsh et al. used TEM to show that there

was no evidence of crystalline phases below 10 V [46]. Vanhumbeeck and Poost's review of the properties of anodic Ti oxide reports that TiO_2 is amorphous and transforms into anatase structure as the oxide thickness increases [10]. The authors claim that the crystallization voltages in the literature show a "very wide range for different experimental conditions and even for apparently identical ones". This is primarily due to how sensitive crystallization is to texture, surface conditions, metal purity, and due to variable sensitivities of the experimental techniques used to detect crystallization [10].

Returning to the discussion of our results in the context of the PDM and HFM mechanisms, in the PDM, the Nernst-Plank equation describes the flux of vacancies via both migration in an electric field and diffusion. On the other hand, interstitial ions moving through the oxide in the HFM case should be able to undergo random exchange with original lattice ions, which we don't observe significant evidence of. No ^{18}O atoms are observed close to the top surface. The broadening of the ^{18}O profiles may indicate the statistical effect of diffusion as a countervailing effect on migration, which leads to oxygen profiles "spreading out".

In the MEIS and NRA profiles in Figs. 5 and 6, the ^{18}O-containing region appears to become increasingly thicker as a function of anodization voltage. At 0 V (as-is), its thickness is ≈ 40 Å and the ^{18}O fraction reaches a maximum of 0.4 at depth ≈ 30 Å. At 10 V the region is ≈ 170 Å thick and the ^{18}O fraction reaches a maximum of 0.15 at depth ≈ 295 Å.

Another effect to consider is called energy straggling that is the process that occurs when H^+ penetrate the oxide films and stochastically interact with the electrons orbiting the medium's atoms leading to a "spreading out" of the initially mono-energetic beam in a Gaussian fashion. The greater the thickness of $Ti^{16}O_2$ that the H^+ must traverse before encountering $Ti^{18}O_2$, the higher the statistical uncertainty in beam energy and the more significant the degradation in depth resolution, which leads to a broadening effect of the depth profiles. For NRA and MEIS, the uncertainty in the ion beam incident energy is ± 0.2 keV. The product of the uncertainty of the beam energy with the H^+ energy loss (for between 150 and 200 keV), translates into a depth uncertainty of about ± 10.7 Å. This may also account for why, for anodization voltages up to 1.5 V, the NRA ^{18}O distributions appear wider than the MEIS depth profiles and for the differences in ^{18}O peak position and ^{18}O fraction between the two techniques. Nonetheless, the ^{18}O peak positions are equal for the uncertainties involved. For 2–10 V, the ^{18}O is distributed over a wider range and the uncertainty in the depth scale is less important in these samples given the larger depth they cover. The summed ^{18}O areal densities as measured by both techniques are equal within experimental uncertainties and constant over all anodization voltages (Fig. 7).

Another factor in favour of the PDM is the good agreement between the ion beam analysis (IBA) techniques (MEIS and NRA) related to the
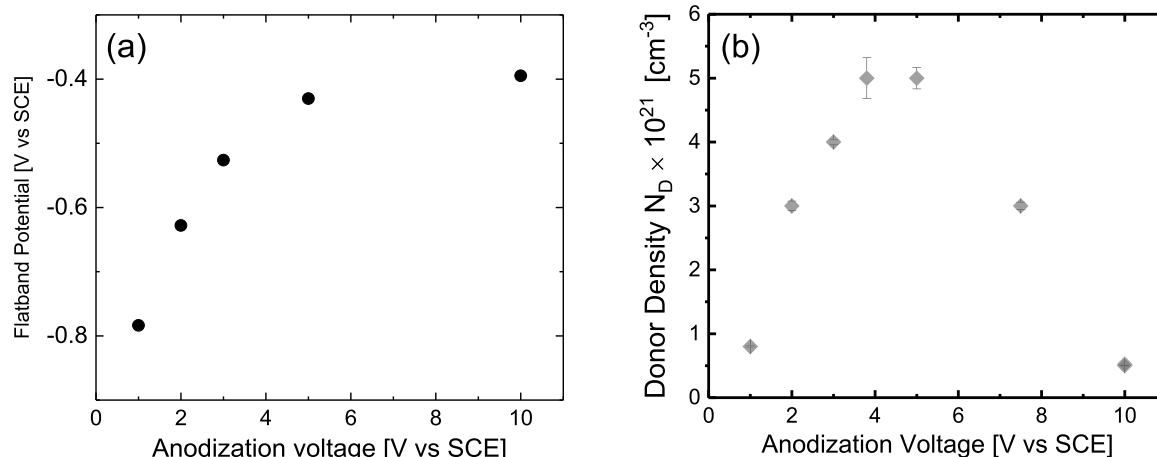

Fig. 11. (a) Calculated flat band potential, and (b) calculated donor density of the passive films formed on anodized Ti specimens in 0.27 M NaCl solution at 21 °C.

evolution of the oxide films. Both show that the surface position of the ^{16}O region remains unchanged while its width grows monotonically as a function of voltage and they show that the ^{18}O region is always adjacent to the unoxidized metal. From the MEIS spectra, the $Ti^{16}O_2$ region increases from 10 Å (0 V) to 155 Å (10 V). The stoichiometry of the oxide can be described as $Ti^{16}O_{2-x}^{18}O_x$, where x increases with increasing depth eventually approaching a value of 2 (i.e., we reach regions no longer containing ^{16}O isotope at all). Past the region of isotopic mixing there is a sub-oxide region that contains only ^{18}O, which represents the furthest depth to which O has been transported. The IBA depth profiles are evidence of a bi-layer oxide structure of the form: $Ti^{16}O_2/Ti^{18}O_2/Ti$. This bi-layer structure is a major prediction of the PDM which required the ^{18}O in the original passive-oxide always be located adjacent to the Ti metal and the ^{16}O-containing regions between that and the electrolyte.

The observed evolution of the anodic film compositions overall contradicts the predictions of the HFM that instead predicted that the original ^{18}O region would be sandwiched between the two newly-grown ^{16}O regions, i.e. $Ti^{16}O_2/Ti^{18}O_2/Ti^{16}O_2/Ti$. The only way how the HFM can predict our observed bi-layer structure is for the mobility of the O ions to be zero ($t_O = 0$) or negligibly small compared to Ti interstitial ion transport ($t_{Ti} = 1$). If we compare these results to the values of gas-phase diffusivities for n-type TiO_{2-x}, fast Ti cationic diffusion ($D_o = 2 \times 10^{-6}$ m^2/s) was reported with activation energies of 2.1–2.8 eV [47]. Lower ^{18}O diffusion coefficient for coarse grained TiO_2 was reported ($D_o = 2 \times 10^{-7}$ m^2/s), and even lower values for nanocrystalline TiO_2 for diffusion *via* grain boundaries ($D_o = 1.4 \times 10^{-8}$ m^2/s)[5]. In other words, if the mobility of Ti ions is a factor of ~100 higher compared to O ion mobility, top surface $Ti^{16}O_2$ layer growth will dominate and therefore HFM cannot be excluded completely.

As far as the authors are aware, there is a single other study that performs depth profiling of anodized Ti and relates these profiles to specific predictions of the PDM and HFM. Tun et al. anodized Ti electrodes (thin foils) with pre-existing air-grown oxide in aqueous NaCl, and probed them non-destructively using *in-situ* neutron reflectometry (NR). After anodization the oxide could be divided into two distinct regions: an outer one containing significant amounts of hydrogen (which has a high cross section in NR), and an inner region which had the same thickness as the original air-grown oxide. This bi-layer structure has led the authors to also select the PDM as a preferred model of anodization [22].

Another important prediction of the PDM is that steady-state oxide thickness is a linear function of voltage under steady state conditions [23]:

$$L_{ss} = \frac{1-\alpha}{\varepsilon_L} V + B \qquad (3)$$

where, α is the polarizability of the solution/oxide interface, B is a constant that depends on pH and on rate constants for film formation and film dissolution, and ε_L is the mean electric field. The slope of the line in Fig. 7, known as the "anodization ratio" is 24.5±0.6 ÅV^{-1}. This is in agreement with 25.4 ÅV^{-1} as determined by *in-situ* neutron reflectometry for Ti electrodes in aqueous NaCl solution [22] and 23.4 ÅV^{-1} determined by Khalil and Leach using α spectrometry [16]. Higher anodization ratios of 41.5 ÅV^{-1} and 51.5 ÅV^{-1} were reported for annealed and nano-grained Ti foils anodized in Hank's physiological solution at 37 °C [48]. If we assume polarizability of the solution/oxide interface $\alpha = 0.5$, the electric field strength for amorphous TiO_2 films grown at 0-10 V is calculated to be 2.04×10^6 V/cm. The latter value is in good agreement with the electrical field strength (1.73×10^6 V/cm) found in the previous MS modelling [20], for anodic TiO_2 films grown in 0.5 M H_2SO_4. Furthermore, considering our Mott–Schottky observations of the changes in the carrier densities at ~ 4 V (Fig. 11(b)), and observation of the second time constant at ~3.65 V (Fig. 9(c)), we can apply a linear fit to steady-state oxide thicknesses in the 0–2 V range, Fig. 7(a), to obtain a slightly higher anodization ratio of 31±3 Å V^{-1}.

4. Conclusions

In the present study, an oxygen isotopic labeling procedure in conjunction with high-resolution ion depth profiling (NRP and MEIS) and Mott–Schottky analysis (MS), was used to study the anodic oxide growth mechanisms on a Ti sample in 0.27 M NaCl solution at 21 °C. Ultra-thin Ti films were exposed to $H_2^{18}O$ *in-situ* to create passive oxide films, which were then anodized in $D_2^{16}O$, resulting in a bi-layer structure with two distinct oxide regions, $Ti^{16}O_2/Ti^{18}O_2/Ti/Si(001)$ for the entire range of anodization voltages (0–10 V). The outermost region, consisting of $Ti^{16}O_2$, was consistently adjacent to the oxide/solution interface, while the $Ti^{18}O_2$ region grew directly into the Ti metal and contained all the $Ti^{18}O_2$ which composed the original passive oxide. The interpretation of these results is in favour of the point defect model (PDM) as an explanation of the mechanism for oxide growth. HFM may to be still valid under conditions when Ti ions are much faster than O ions, and $Ti^{16}O_2/Ti^{18}O_2/Ti^{16}O_2/Ti$ structure predicted by HFM will become $Ti^{16}O_2/Ti^{18}O_2/Ti$ structure.

Our experimental anodization ratio is 24.5±0.6 Å V^{-1} and this is in agreement with 25.4 Å V^{-1} as determined by *in-situ* neutron reflectometry for Ti electrodes in aqueous NaCl solution [22] and 23.4 ÅV^{-1} determined by Khalil and Leach using α spectrometry [16]. Mott–Schottky (MS) analyses show positive slopes, indicating formation of an *n*-type TiO_2 semiconductor, with O vacancies (or Ti interstitials) as major carriers in the 0–4 V range. Charge carrier densities, $N_D = 0.8$-5.0×10^{21} cm^{-3} were calculated from Mott–Schottky analysis. We observed an increase in the charge carrier density over the range of 0–4 V, followed by a decrease at higher voltages; the latter may be attributed to a change in the passive oxide crystalline structure, or defect annihilation. Initially either O vacancies or Ti interstitials are injected into oxide at the interface and can play a major role in the passive oxide growth, while at higher voltages (above ~3.5-4.0 V), cationic point defects (e.g. O interstitials) may contribute to the growth mechanism.

CRediT authorship contribution statement

M. Brocklebank: Formal analysis, Data curation, Methodology, Writing – original draft. **H. Feltham:** Data curation, Formal analysis, Visualization, Writing – review & editing. **J.J. Noël:** Methodology, Conceptualization, Funding acquisition, Supervision, Writing – review & editing. **L.V. Goncharova:** Conceptualization, Supervision, Funding acquisition, Methodology, Visualization, Writing – review & editing.

Declaration of Competing Interest

The authors declare that they have no known competing financial interests or personal relationships that could have appeared to influence the work reported in this paper.

Acknowledgments

Supplementary materials

Supplementary material associated with this article can be found, in the online version, at doi:10.1016/j.electacta.2022.141342.

References

[1] N.K. Kuromoto, R.A. Simão, G.A. Soares, Titanium oxide films produced on commercially pure titanium by anodic oxidation with different voltages, Mater. Charact. 58 (2007) 114–121.

[2] J. Alipal, T. Lee, P. Koshy, H. Abdullah, M. Idris, Evolution of anodised titanium for implant applications, Heliyon 7 (7) (2021) e07408.

[3] X. Cui, H.M. Kim, M. Kawashita, L. Wang, T. Xiong, T. Kokubo, T. Nakamura, Preparation of bioactive titania films on titanium metal via anodic oxidation, Dent. Mater. 25 (2009) 80–86.

[4] L. Wu, J. Liu, M. Yu, S. Li, H. Liang, M. Zhu, Effect of anodization time on morphology and electrochemical impedance of anodic oxide films on titanium alloy in tartrate solution, Int. J. Electrochem. Sci 9 (2014) 5012–5024.

[5] D. Regonini, C.R. Bowen, A. Jaroenworaluck, R. Stevens, A review of growth mechanism, structure and crystallinity of anodized TiO$_2$ nanotubes, Mater. Sci. Eng. R Rep. 74 (2013) 377–406.

[6] Y.H. Hsien, C.F. Chang, Y.H. Chen, S. Cheng, Photodegradation of aromatic pollutants in water over TiO$_2$ supported on molecular sieves, Appl. Catal. B Environ. 31 (2001) 241–249.

[7] G. Wang, Hydrothermal synthesis and photocatalytic activity of nanocrystalline TiO$_2$ powders in ethanol–water mixed solutions, J. Mol. Catal. A Chem. 274 (2007) 185–191.

[8] S. Sahni, S.B. Reddy, B. Murty, Influence of process parameters on the synthesis of nano-titania by sol–gel route, Mater. Sci. Eng. A 452 (2007) 758–762.

[9] M. Erol, T. Dikici, M. Toparli, E. Celik, The effect of anodization parameters on the formation of nanoporous TiO$_2$ layers and their photocatalytic activities, J. Alloys Compd. 604 (2014) 66–72.

[10] J.F. Vanhumbeeck, J. Proost, Current understanding of Ti anodisation: functional, morphological, chemical and mechanical aspects, Corros. Rev. 27 (2009) 117–204.

[11] M. Lohrengel, Thin anodic oxide layers on aluminium and other valve metals: high field regime, Mater. Sci. Eng R Rep. 11 (1993) 243–294.

[12] A. Güntherschulze, H. Betz, Die Bewegung der Ionengitter von Isolatoren bei extremen elektrischen Feldstärken, Zeitschrift für physik 92 (1934) 367–374.

[13] E. Verwey, Electrolytic conduction of a solid insulator at high fields. The formation of the anodic oxide film on aluminium, Physica 2 (1935) 1059–1063.

[14] N. Cabrera, N. Mott, Theory of the oxidation of metals, Rep. Prog. Phys. 12 (1949) 163.

[15] J. Davies, B. Domeij, J. Pringle, F. Brown, The migration of metal and oxygen during anodic film formation, J. Electrochem. Soc. 112 (1965) 675.

[16] N. Khalil, J. Leach, The anodic oxidation of valve metals—I. Determination of ionic transport numbers by α-spectrometry, Electrochim. Acta 31 (1986) 1279–1285.

[17] D.D. Macdonald, Passivity–the key to our metals-based civilization, Pure Appl. Chem. 71 (1999) 951–978.

[18] C. Chao, L. Lin, D. Macdonald, A point defect model for anodic passive films: I. Film growth kinetics, J. Electrochemi. Soc. 128 (1981) 1187.

[19] D.D. Macdonald, M. Urquidi-Macdonald, Theory of steady-state passive films, J. Electrochem. Soc. 137 (1990) 2395.

[20] B. Roh, D.D. Macdonald, Passivity of titanium: part II, the defect structure of the anodic oxide film, J. Solid State Electrochem. 23 (2019) 1967–1979.

[21] M. Aliofkhazraei, D. Macdonald, E. Matykina, E. Parfenov, V. Egorkin, J. Curran, S. Troughton, S. Sinebryukhov, S. Gnedenkov, T. Lampke, Review of plasma electrolytic oxidation of titanium substrates: mechanism, properties, applications and limitations, Appl. Surf. Sci. Adv. 5 (2021), 100121.

[22] Z. Tun, J. Noel, D. Shoesmith, Electrochemical modification of the passive oxide layer on a Ti film observed by in situ neutron reflectometry, J. Electrochem. Soc. 146 (1999) 988.

[23] D.D. Macdonald, The history of the point defect model for the passive state: a brief review of film growth aspects, Electrochim. Acta 56 (2011) 1761–1772.

[24] T. Akermark, The use of oxygen isotopic labeling to understand oxidation mechanisms, Oxid. Met. 50 (1998) 167–188.

[25] S. Basu, J. Halloran, Tracer isotope distribution in growing oxide scales, Oxid. Met. 27 (1987) 143–155.

[26] H. Lu, T. Gustafsson, E. Gusev, E. Garfunkel, An isotopic labeling study of the growth of thin oxide films on Si (100), Appl. Phys. Lett. 67 (1995) 1742–1744.

[27] J. Wilson, D. Schwartz, S.B. Adler, Nonlinear electrochemical impedance spectroscopy for solid oxide fuel cell cathode materials, Electrochim. Acta 51 (2006) 1389–1402.

[28] A.J. Bard, L.R. Faulkner. Electrochemical Methods: Fundamentals and Applications, 2nd ed., Wiley, 2001.

[29] M.E. Orazem, B. Tribollet. Electrochemical impedance spectroscopy, Wiley, Pennington, NJ, 2008.

[30] X. He, J.J. Noël, D.W. Shoesmith, Temperature dependence of crevice corrosion initiation on titanium grade-2, J. Electrochem. Soc. 149 (2002) B440.

[31] J. Noel, D. Shoesmith, B. Ikeda, Crevice corrosion of alpha titanium alloys, localized corrosion, in: Proceedings of the Topical Research Symposium, CORROSION/2001, eds. GS Frankel, JR Scully, NACE, Houston, TX, 2001, p. 65, 2001.

[32] L.V. Goncharova, M. Dalponte, T. Gustafsson, O. Celik, E. Garfunkel, P.S. Lysaght, G. Bersuker, Metal-gate-induced reduction of the interfacial layer in Hf oxide gate stacks, J. Vac. Sci. Technol. A 25 (2007) 261–268.

[33] L.V. Goncharova, M. Dalponte, T. Gustafsson, E. Garfunkel, P.S. Lysaght, B. Foran, J. Barnett, G.I. Bersuker, Oxygen diffusion and reactions in Hf-based dielectrics, Appl. Phys. Lett. 89 (2006), 044108.

[34] J. Kim, W. Lennard, C. McNorgan, J. Hendriks, I. Mitchell, D. Landheer, J. Gredley, Depth profiling of ultrathin films using medium energy ion scattering, Curr. Appl. Phys. 3 (2003) 75–82.

[35] T. Nishimura, Computer simulation program for medium-energy ion scattering and Rutherford backscattering spectrometry, Nucl. Instrum. Methods Phys. Res., Sect. B 371 (2016) 97–100.

[36] Y. Wang, M. Nastasi. Handbook of modern Ion beam materials analysis, Research Society, 2009.

[37] N. Fairley, CasaXPS VAMAS processing software, Available from World Wide Web: http://www.casaxps.com, (2010).

[38] M. Brocklebank, S.N. Dedyulin, L.V. Goncharova, Stopping cross sections of protons in Ti, TiO$_2$ and Si using medium energy ion scattering, Eur. Phys. J. D 70 (2016) 7.

[39] A. Burke, C. Brown, W. Bowling, J. Glaub, D. Kapsch, C. Love, R. Whitaker, W. Moddeman, Ignition mechanism of the titanium–boron pyrotechnic mixture, Surf. Interface Anal. 11 (1988) 353–358.

[40] D. Gonbeau, C. Guimon, G. Pfister-Guillouzo, A. Levasseur, G. Meunier, R. Dormoy, XPS study of thin films of titanium oxysulfides, Surf. Sci. 254 (1991) 81–89.

[41] B. Siemensmeyer, K. Bade, J. Schultze, XPS and electrochemical studies of thin TiN layers, Berichte der Bunsengesellschaft für physikalische Chemie 95 (1991) 1461–1469.

[42] L. Wang, H. Yu, K. Wang, H. Xu, S. Wang, D. Sun, Local fine structural insight into mechanism of electrochemical passivation of titanium, ACS Appl. Mater. Interfaces 8 (2016) 18608–18619.

[43] G. Ansari, A. Fattah-Alhosseini, On the passive and semiconducting behavior of severely deformed pure titanium in Ringer's physiological solution at 37° C: a trial of the point defect model, Mater. Sci. Eng. C 75 (2017) 64–71.

[44] B. Munirathinam, R. Narayanan, L. Neelakantan, Electrochemical and semiconducting properties of thin passive film formed on titanium in chloride medium at various pH conditions, Thin Solid Films 598 (2016) 260–270.

[45] V. Kumaravel, S. Mathew, J. Bartlett, S.C. Pillai, Photocatalytic hydrogen production using metal doped TiO$_2$: a review of recent advances, Appl. Catal. B Environ. 244 (2019) 1021–1064.

[46] J. Marsh, D. Gorse, A photoelectrochemical and AC impedance study of anodic titanium oxide films, Electrochim. Acta 43 (1998) 659–670.

[47] K. Hoshino, N. Peterson, C. Wiley, Diffusion and point defects in TiO$_{2−x}$, J. Phys. Chem. Solids 46 (1985) 1397–1411.

[48] A. Fattah-Alhosseini, O. Imantalab, G. Ansari, The role of grain refinement and film formation potential on the electrochemical behavior of commercial pure titanium in Hank's physiological solution, Mater. Sci. Eng. C 71 (2017) 827–834.